Materials Characterization 185 (2022) 111718

Contents lists available at ScienceDirect

Materials Characterization

journal homepage: www.elsevier.com/locate/matchar

Influence of nanoscale defects on the improvement of photocatalytic activity of Ag/ZnO

L. Muñoz-Fernandez [a,*], L.S. Gomez-Villalba [b], O. Milošević [c], M.E. Rabanal [a,*]

[a] University Carlos III of Madrid Department of Materials Science and Engineering and Chemical Engineering and IAAB, Avda. Universidad 30, 28911 Leganés, Madrid, Spain
[b] Instituto de Geociencias (CSIC, UCM), C/Doctor Severo Ochoa 7, 28040 Madrid, Spain
[c] Institute of Technical Sciences of the Serbian Academy of Sciences and Arts, Knez Mihailova 35/IV, 11000 Belgrade, Serbia

ARTICLE INFO

Keywords:
Ag/ZnO
Nanostructured system
Nanoscale defects
Solvothermal method
Photocatalysis

ABSTRACT

This study presents the advances in the field of ZnO/Ag catalysts from the synthesis of hierarchical ZnO nanowires (NWs) decorated with Ag nanoparticles, prepared by a facile solvothermal method at 120°C. It evaluates the photocatalytic efficiency from studying the time reaction of Ag/Zn concentration ratio and the presence of cetyltrimethylammonium bromide (CTAB) as an organic dispersant. X-ray diffraction, scanning electron microscopy, and analytical/high-resolution transmission electron microscopy results confirmed the presence of homogeneous cylindrical ZnO nanowires and quasi-spherical Ag crystals. ZnO NWs exhibited hexagonal wurtzite structure and cubic FCC symmetry in Ag nanoparticles (NPS). Two types of nanostructures, including homogeneous cylindrical ZnO NWs in the absence of Ag and simultaneous presence of ZnO NWs and Ag NPs, formed depending on experimental conditions. The photocatalytic activity was evaluated by studying methylene blue (MB) degradation time under UV light excitation. Diffuse reflectance UV–Vis spectrophotometry (UV–Vis DRS) allowed identifying the ZnO absorption band at ~393 nm. Crystal size varied depending on the reaction time and the addition of CTAB. Synthesis time increased bandgap values, getting better photocatalytic performance in samples synthesized in intermediate times (6 h), higher Ag^{+}/Zn^{2+} molar ratio (0.2/1.0), and CTAB. According to HRTEM observations, the presence of silver nanocrystals with high content of defects (twinning, stacking faults) could play an essential role in the photocatalytic response. In this context, the specific synthesis conditions of Ag/ZnO might be more appropriate for their use in organic dyes degradation in water and the potential use in protective treatments against materials biodeterioration processes.

1. Introduction

Nowadays, the alarming increase in industrial pollution levels due to new technologies is becoming more critical. Unfortunately, effluents containing many organic pollutants are released into the environment, reaching the surface and groundwater. Most of these compounds do not degrade by themselves, causing a significant social problem for environmental pollution. The use of traditional pollutant adsorption methods only transfers pollutants from one substance (e.g., water) to another (e.g., carbon active [1]). Nanotechnology has become one of the most active research fields because of its unique properties and potential technological applications [2]. Besides, photocatalysis is a promising technology for harvesting clean solar energy using hydroxyl radicals to react with the environmental pollutant dye, making it an environmentally harmless substance [3]. Solar energy allows purifying the polluted wastewater by using nanomaterials [2]. The design of these materials is commonly selected among different synthesis methods and subsequently evaluated based on their photocatalytic behavior as reported in several materials based on semiconductors (such as WO_3, CdS, TiO_2, and ZnO) [2,4,5], [6]. Moreover, nanostructured materials deserve special attention since they provide superior properties compared to their counterparts at bulk scale [7,8]. Among these nanostructured photocatalysts, TiO_2 and ZnO are the most studied materials [9–13]. Recent studies have confirmed that ZnO presents a better efficiency than TiO_2 in photocatalytic degradation of some dyes, even in aqueous solution, since ZnO can absorb a more significant portion of the UV light [14].

* Corresponding authors.
E-mail addresses: lidia.mf.profesora@gmail.com (L. Muñoz-Fernandez), luzgomez@geo.ucm.es (L.S. Gomez-Villalba), olivera.milosevic@itn.sanu.ac.rs (O. Milošević), mariaeugenia.rabanal@uc3m.es, eugenia@ing.uc3m.es (M.E. Rabanal).

https://doi.org/10.1016/j.matchar.2021.111718
Received 18 July 2021; Received in revised form 30 December 2021; Accepted 31 December 2021
Available online 7 January 2022

Zinc oxide (ZnO) is a heterogeneous semiconductor photocatalyst with a broad and direct bandgap of 3.37 eV at room temperature [8]. ZnO system presents three polymorphic structures of which only the hexagonal wurtzite is thermodynamically stable under ambient conditions [15,16]. This semiconducting oxide exhibits many applications, especially in photocatalysis, as described earlier. ZnO absorbs photons, and electrons from the valence band shift to the conduction band in the presence of a suitable light source, leaving an equal number of holes in the valence band behind. This is known as "e^--h^+ pair" [17,18]. When this charge separation is maintained, the photogenerated electron-hole pair participates in a redox reaction leading to the "in situ" formation of hydroxyl radicals and is responsible for removing organic pollutants present in water [19,20]. The photogenerated electrons react with dissolved O_2 molecules forming the superoxide anion radicals ($O_2^{-\bullet}$), while holes react with H_2O, leading to hydroxyl radicals ($OH^\bullet$). Under the high redox potential of hydroxyl radicals, dye molecules are oxidized to CO_2, H_2O, and mineral acids. However, the rapid recombination of photo-excited electrons and holes reduces its photocatalytic efficiency. One of the most efficient methods to overcome this problem is to add noble metals with complementary properties to form core-shell, hetero-, or doped structures [21,22]. Besides the fact that ZnO is chemically and thermally stable, these functional properties make it a suitable and valuable alternative to industrial-scale applications such as air purification, disinfection, and waste treatment [23].

Several studies report the influence of local defects and impurities [14,24,25] on the ZnO morphology as well as the type of dopant [26,27]. Most of them study the functional properties, which depend on the type and amount of dopant [28–30]. In that case, several works attempt to synthesize materials of ZnO with noble metals on their surface, improve the photocatalytic activity, enhance the corrosion resistance, and increase the photo-stability during the photocatalytic process [31,32]. Among them, Ag NPs could appear to be promising based on their size and energy levels [33,34].

Different researches point out that Ag–ZnO photocatalysts are better than pure ZnO for two reasons: (i) the nanostructures present the largest surface area, which leads to enhance adsorption of the pollutant; (ii) the cationic silver reacts with free electrons from the conduction band as electron sinks to decrease the electron/hole recombination rate [8,34].

Similarly, ZnO and Ag have biocides properties to control deterioration in various materials. Besides, they have bactericidal and antifungal properties, achieving significant advances in different fields of application, highlighting their biomedical applications [35,36]. Combining these two compounds is strategic to improve the efficiency for biological colonization control, which causes damage and loss of cohesion in construction or fine arts materials, among others, many of them from cultural heritage [37,38].

Among the different methods for the synthesis of ZnO, the most common are chemical vapor deposition (CVD), vapor transport, ultrasonic-assisted [39], sol-gel process [40], precipitation [41], and solvothermal [42]. However, the last one is widely common due to its simplicity and low cost, making this process more accessible, less expensive, and suitable for large-scale production than other approaches [8,43].

Control of ZnO particle morphology is also a determining factor because it plays a significant role in magnetic, electrical, optical, photocatalytic, and other properties [44–48]. Modifications in particle nucleation and growth in the solvothermal process are possible by introducing organic additives in the reaction media so that it is possible to control the morphology and size [33]. Cetyltrimethylammonium bromide (CTAB) is currently used as an organic dispersant to prepare ZnO nanostructures [49,50]. The precise actuation mechanism is still in the study. Some authors consider that, due to the synergic effect of surfactant (CTAB) and solvent (common ethanol), the generation of active sites on the ZnO surface is favored by the interaction of CTAB with growth units, so that ZnO nanowires are created from those sites [43], [51–53].

Despite the constant advances in synthesis methods that seek to improve the properties of Zn / Ag Nps or know the nanoscale structures [54], there is a need to evaluate the role of defects and the possible modifications at the atomic level in the photocatalytic efficiency. Therefore, this work analyzes the presence of defects at the atomic level and how they affect the photocatalytic activity of ZnO /Ag Nps synthesized by a solvothermal synthesis method, in short times, low cost, and at low temperatures.

2. Experimental section

2.1. Materials

All the chemical reagents used in the synthesis procedure: zinc nitrate hexahydrate ($Zn(NO_3)_2{\cdot}6H_2O$, purity >99%, Sigma-Aldrich), silver nitrate ($AgNO_3$, purity >98%), Sigma-Aldrich), sodium hydroxide (NaOH, Sigma-Aldrich), ethanol (C_2H_6O), and cetyltrimethylammonium bromide, CTAB ($C_{19}H_{42}BrN$), were used as received, without further purification. High-purity deionized (DI) (18 $M\Omega{\cdot}cm^{-1}$) water obtained by a water purification system (Barnstead, Dubuque, IA, USA) was used as a washing agent.

2.2. Synthesis of Ag/ZnO nanoparticles

Ag/ZnO nanostructures were synthesized via a facile solvothermal method. The precursors, $Zn(NO_3)_2{\cdot}6H_2O$ and $AgNO_3$, were dissolved in pure ethanol as the solvent and sodium hydroxide as a basic agent [42]. Besides, different synthesis times and precursor concentrations were changed to evaluate the effect of these parameters in forming Ag/ZnO hierarchical nanostructures fixing the reaction temperature at 120°C. Table 1 summarizes the reaction conditions.

For a typical preparation process, an amount of $Zn(NO_3)_2{\cdot}6H_2O$, $AgNO_3$ (Table 1), and cetyltrimethylammonium bromide (CTAB) as a dispersant (where it has been appropriate) were added to 20 ml of high-purity ethanol. The solution was stirred at room temperature (RT) for 10 min. After that, 7.5 mmol of NaOH was added to the previous solution stirring for 60 min more. Then, the mixture was transferred into a Teflon autoclave reactor of 75 ml maximum capacity, which was placed inside a stainless steel container to seal tightly. The solvothermal reactor was introduced into the oven at 120°C and at different reaction times (Table 1). Subsequently, the formed precipitates were collected and washed several times by centrifugation with pure ethanol and DI water. Finally, the sample is dried in an air atmosphere at 80°C overnight. Pure ZnO nanostructures without metallic silver nanoparticles were also synthesized by an identical experimental process to compare the behavior of prepared hybrid materials (Table 1).

2.3. Characterization methods

To study the crystal structure, purity, and elemental composition of Ag/ZnO nanostructures, X-ray diffraction (XRD) was carried out by an X-ray diffractometer (Philips Xpert) with Cu K_α radiation (40 kV, 40 mA). The average crystallite size (CS) has been calculated by Scherrer's formula, $D = k{\cdot}\lambda/(\beta_D{\cdot}\cos\theta)$, where λ is the wavelength of the X-ray radiation (in Å), K is a constant taken as 0.9, β_D the full width at half-

Table 1
Synthesis conditions of Ag/ZnO nanostructures at 120°C.

Sample	Reaction conditions			
	$[Zn^{2+}]$ (M)	$[Ag^+]$ (M)	Time (h)	CTAB* (mg)
I		–	6	–
II	$1.85{\cdot}10^{-2}$			6.3
III		$3.75{\cdot}10^{-3}$	18	
IV	$3.75{\cdot}10^{-2}$			–

* CTAB = cetyltrimethyl ammonium bromide ($C_{19}H_{42}BrN$) as dispersant.

maximum height (FWHM) and θ is the diffraction angle (in rad) used in calculus. The samples' most intensive reflection peaks were used in the line broadening analysis [55]. Bragg's law, $n\lambda = 2{\cdot}d{\cdot}\sin\theta$, and the three most intensive reflection peaks of the samples have been used for the lattice parameter calculus of the different phases present in the samples. The morphology, particle size, and chemical composition of Ag/ZnO nanostructures were examined by scanning electron microscopy (SEM, Philips XL 30/EDAX-Dx4) equipped with an energy dispersive X-ray detector (EDS). The samples dispersed in acetone and deposited several drops of this suspension on an aluminum SEM stub. Finally, the stub was dried in air at RT and coated with a thin gold layer to avoid charging before characterization. Analytical Transmission Electron Microscopy (TEM) combined with the Selected Area Electron Diffraction (SAED) study was performed on a JEOL JEM 2100 instrument operated at an accelerating voltage of 200 kV. Previously samples were ultrasonically dispersed in acetone and deposited on a holey carbon copper grid. The High-resolution transmission electron microscopy (HRTEM) study was carried out on a JEOL JEM 3000 FEG microscope operating at 300 kV with a resolution of 0.17 nm point to point. The Digital Micrograph™ (DM, GatanInc.) software was used for the TEM-HRTEM interpretation. The HRTEM observations include a combination image-calculated Fast Fourier transformed (FFT) for structural interpretation and phase identification. The analytical TEM was used to study morphology and analyze the particle size distribution. To every sample, dimensions of at least 25 nanoparticles chosen randomly were measured, and its standard deviations were estimated. An inductively coupled plasma-atomic emission spectrometer (ICP-AES, SpectrAA 220, Varian) analyzed the elemental composition. Ultraviolet-visible (UV–vis) diffuse reflectance spectra (DRS) were recorded by a Perkin-Elmer (Lambda 14P) spectrophotometer using a 60-mm integrator sphere in the diffuse reflectance mode (R) and with $BaSO_4$ as a pattern, over the wavelength range of 250–700 nm. Spectra were registered at RT, and the data were treated by transformation through the Kubelka-Munk function: $F(R) = (1 - R_\infty)^2 / 2R_\infty$, where R_∞ is the reflectance of samples [53]. Brunauer–Emmett–-Teller (BET) surface area measurements were performed in a Micromeritics Gemini VII instrument using N_2 as sorbate (at −196.6°C). Before analysis, the samples were outgassed at 90°C overnight.

2.4. Evaluation of photocatalytic activities (PCA)

The photocatalytic activity (PCA) of Ag/ZnO was evaluated by the methylene blue degradation (MB) in an aqueous solution at room temperature, under UV light, as a model dye photodegradation [56]. In every experiment, a fixed amount of photocatalyst (5 mg) was added to MB aqueous solution (2.5 ppm) in a 600 ml Pyrex glass reactor. Before the irradiation, each suspension was magnetically dispersed by agitation for 40 min in the dark to get the adsorption/desorption equilibrium (between catalyst and dye). The photocatalytic degradation was tested in continuous stirring under UV-light irradiation using a 125 W high-pressure mercury vapor lamp (Jinfei Company, Shanghai) in a dark room. Then, 3 ml of the aliquots were extracted at time intervals fixed. Finally, the UV–Vis spectrometer was used to determine the MB reduction. Also, a blank experiment was carried out in identical measurement conditions as mentioned above to compare the MB decomposition of ZnO.

3. Results and discussion

3.1. X-ray diffraction (XRD)

Fig. 1 shows the XRD patterns of the pure ZnO (sample I) and Ag/ZnO (sample II, III and IV) nanostructures respectively. The diffraction peaks of the sample I were indexed to a single-phase ZnO with a hexagonal wurtzite structure (Joint Committee on Powder Diffraction Standards, JCPDS card no.: 89-1397) without any other crystalline phases [46]. Concerning the Ag/ZnO nanostructures, it was found that the diffraction peaks, both in their peak position and their relative intensity, were in complete agreement with the standard spectrum of ZnO (JCPDS no.: 89-1397) and metallic face-centered-cubic (fcc) Ag structure (JCPDS standard card no.: 87-0720), indicating the formation of Ag as the second phase. Silver diffraction peaks at 2θ of 38.1, 44.5, and 64.5 in the samples II, III and IV indicate the metallic crystalline phase formation beside the pure zinc oxide phase. Furthermore, no evidence of other diffraction peaks related to Ag_2O, AgO were detected in the patterns. Similar to Xu et al. [45] and Wu et al. [42], our XRD results

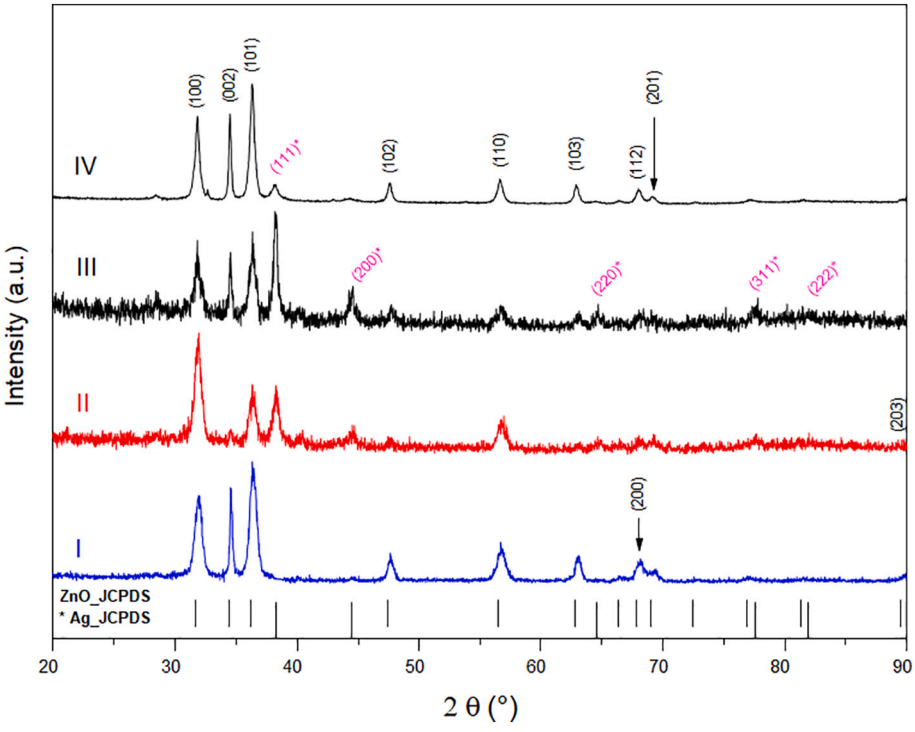

Fig. 1. XRD patterns of ZnO (sample I) and Ag/ZnO nanostructures (sample II, III and IV).

indicate that impurities and other crystalline reaction phases are not present apart from ZnO and Ag.

Comparing the XRD pattern of pure ZnO (sample I) with the reference card no.: 89-1397, the diffraction pattern presents an inversion of the relative intensity of the diffraction peak corresponding to $2\theta = 31.74°$. This inversion could imply a preferential growth orientation in the (002) plane without Ag NPs. However, in the samples II, III and IV prepared in the presence of $AgNO_3$, the diffraction peaks of ZnO showed relative intensities similar to the standard XRD with a hexagonal wurtzite structure (reference card no.: 89-1397). Concerning silver diffraction peak intensity increasing [Ag]/[Zn] ratio, a consistent increase in the intensity of silver peaks can be noted. Besides, it should be noted that the peak positions of the ZnO phase are not shifted, which suggests any partial substitutional incorporation of Ag^+ ions at the ZnO lattice. This issue could presumably be related to the ionic size difference between Ag^+ (0.115 nm) and Zn^{2+} (0.074 nm).

Table 2 shows the calculated cell parameters of the pure ZnO sample and those decorated with silver. No significant changes were observed in the sample I compared with reference card no.: 89-1397. However, in the case of samples II and III ($[Ag^+]/[Zn^{2+}] = 0.2$), the calculated lattice parameters are slightly lower than the JCPDS card. It is essential to emphasize the considerable difference between ionic radii of Zn^{2+} (0.74 Å) and Ag^+ (1.15 Å) [57], which limits the replacement of the Zn^{2+} sites or interstitial sites by Ag^+ in the ZnO lattice [31]. In fact, the ionic radio of Ag^+ is larger than that of Zn^{2+}. Thus a dilatation of the "c" and "a" axe should be observed according to a shift of diffraction peaks. From these findings, it can be deduced that no diffusion phenomena of silver ions within the ZnO structure have been observed. Diffusion phenomena reported by Khosravi et al. [58] in Ag-doped ZnO nanoparticles obtained by the sol-gel method showed important modifications in the lattice parameters. However, unlike those results, the variation in this study is not significant, proving that no diffusion phenomena are occurring.

The Crystallite Size (CS, in nm) was estimated from XRD patterns using the Scherrer's formula for pure ZnO (sample I) and Ag/ZnO samples (sample II, III y IV). Table 2 lists the results derived from the most intense indexed peaks (100), (002) and (101) for ZnO and (111), (200) and (220) for metallic Ag NPs.

Table 2 shows that the maximum reduction in the CS to ZnO (crystallite size of sample II = 15 ± 3 nm) was obtained with a shorter reaction time and with the addition of CTAB as a surfactant. As well, it has been confirmed that both the increase of reaction time and the absence of CTAB lead to an enhancement of the CS of metallic silver phase from 14 ± 2 nm to 40 ± 19 nm, and the crystalline phase of ZnO from 15 ± 3 to 28 ± 4 nm. According to the calculated data, reaction time and dispersant presence are more pronounced to metallic Ag NPs than ZnO NWs. Moreover, it is noted (Fig. 2) that the full width at half maximum (FWHM) of the peaks becomes smaller with an increase of synthesis time; besides, FWHM is broader with CTAB addition in the reaction media.

3.2. Scanning electron microscopy (SEM)

High magnification (65,000×) SEM micrographs taken with secondary electrons (SE) detector and their corresponding EDS spectra of synthesized samples (pure ZnO-sample I, II, III and IV) according to the experimental conditions summarised in Table 1 are shown in Fig. 2.

Fig. 2.a shows highly agglomerated and heterogeneous bundles of pure ZnO (sample I) and their respective EDS spectrum. Besides, nanowire morphology (NWs) is suggested and confirmed by the TEM analysis presented below. The semi-quantitative analysis of a selected area (Fig. 2.b) shows that the chemical composition analysis agrees with the pure ZnO phase. All of the peaks on the curves are ascribed to Zn, O, Al, and Au elements, and no peaks of other elements are observed. Al and Au signals come from the sample holder and coating, respectively, which should be ignored.

ZnO NW crystal growth is more evident when adding CTAB as an organic dispersant in reaction media (samples II and III), as shown in Fig. 2.c and 2.e. Also, when the reaction time increased from 6 to 18 h, the morphology and the particle size, observed in sample III (Fig. 2.e) is different from the previous one, sample II (Fig. 2.c), as will be described in the following TEM results. Fig. 2.c shows a similar structure to the pure ZnO morphology with truly agglomerated wire bundles. According to EDS analysis, in the Ag-ZnO nanostructures, silver is detected, besides Zn, Al, Au, and O atoms. However, it is hard to identify the presence of the metallic silver nanoparticles, their morphology, size, shape, and the proper distribution over the ZnO NWs surface due to the resolution limit of this technique. At most ample reaction time, a heterogeneous and agglomerated surface of different NWs in size is observed (Fig. 2.e). Therefore, analogously to sample II, it was impossible to distinguish the particular morphology and shape of metallic silver NPs due to their small size and distribution. Besides, the agglomeration phenomenon caused by the high surface energy of ZnO NWs would hinder the identification of isolated metal silver NPs. [59].

In sample IV synthesized without dispersant (CTAB), it is difficult to identify individual ZnO nanowires. On the contrary, a dense, compact, and highly agglomerated morphology was observed. Likewise, as in the previous samples, silver is also detected by EDS analysis, although the isolated silver NPs could not be detected. Therefore, these results could agree with the XRD as mentioned earlier results (Fig. 1.II and 1.III).

3.3. Transmission electron microscopy

Analytical TEM and HRTEM techniques provide detailed information about microstructure, shape, and morphology (Figs. 3 and 4).

Fig. 3.a shows a representative low-magnified TEM image of sample I (pure ZnO phase). Homogeneous NWs with cylindrical morphology and uniform diameters are observed. However, a bimodal length distribution is determined. Therefore, the average lengths estimated are about 66 ± 10 nm and 138 ± 24 nm. Regarding the width of ZnO NWs, a narrow and homogenous distribution is measured (11 ± 2 nm). Finally, two average aspect ratios (AR = length/width) are obtained (6 ± 2 and 13 ± 4, the

Table 2
Crystallite size (CS, in nm) and lattice parameter determined from Scherrer Formula and XRD patterns, respectively.

Sample	Crystallite size* (nm)		Lattice parameters** (Å)					
	ZnO	Ag	ZnO				Ag	
			JCPDS 89-1397		Calculated.		JCPDS 87-0720	Calculated.
			a	c	A	c	a	
I	27.4 ± 5.5	–	3.253	5.213	3.246 ± 0.003	5.195 ± 0.015	4.077	–
II	15.2 ± 2.7	13.9 ± 1.7			3.244 ± 0.002	5.180 ± 0.012		4.067 ± 0.014
III	23.8 ± 5.8	27.0 ± 7.7			3.239 ± 0.004	5.172 ± 0.023		4.072 ± 0.005
IV	28.4 ± 3.7	40.1 ± 18.8			3.251 ± 0.003	5.210 ± 0.017		4.087 ± 0.019

* Results obtained by the Scherrer's formula ($D=K\lambda/\beta\cos\theta$).
** Results obtained by Bragg's law ($n\lambda = 2d\text{sen}\theta$) and derived from the three most intense indexed peaks.

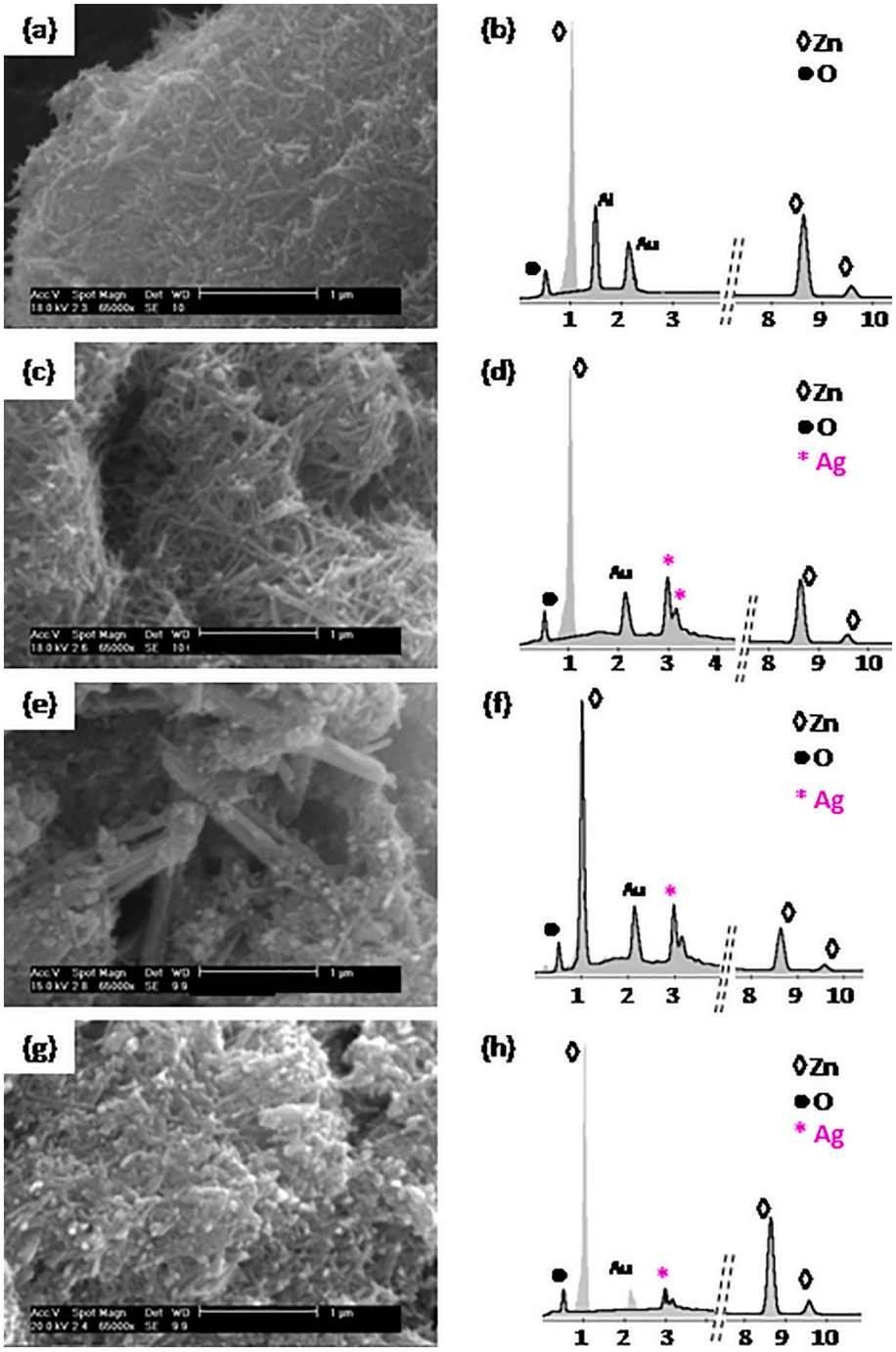

Fig. 2. High magnification (65,000×) SEM images taken with SE detector and the corresponding EDS spectra of Ag/ZnO nanostructures: samples I (a, b), II (c, d), III (e, f) and IV (g, h).

first one being the most representative value). This width corresponds to NWs, which agrees with other authors such as X. Fan et al. [60]. The obtaining of ZnO NWs has evolved into an essential interest since these morphologies offer superior electrochemical properties. Consequently, their dimensional anisotropy results in a more significant number of e^- and h^+ on the active sites and, subsequently, higher activity than spherical morphologies [61].

The semi-quantitative EDS analysis of sample I (Fig. 3.b) confirms the only pure ZnO nanostructured NWs (Si and Cu signals come from sample support). This result is in good agreement with the data of XRD (Fig. 2.I).

The HRTEM image of the dotted rectangle area of the ZnO nanowire (Fig. 3.c) shows the uniform lattice structure and crystalline nature. The ordered crystalline planes with an interplanar spacing of 0.26 nm, corresponding to ZnO's (002) plane with wurtzite structure, were measured. The FFT pattern (inset in Fig. 3.c) also confirms the hexagonal structure of ZnO NWs.

As seen in Fig. 3.d, the SAED ring pattern of pure ZnO NWs confirms its polycrystalline nature. In the pure ZnO sample, the indexed reflections are in agreement with the (100), (101) and (103) planes of the ZnO phase reported in JCPDS standard card no.: = 89-1397. The textured ring pattern suggests a high defect content, particularly in the (101) intensity plane.

Fig. 4 represents the low (Fig. 4.a) and high-resolution TEM images

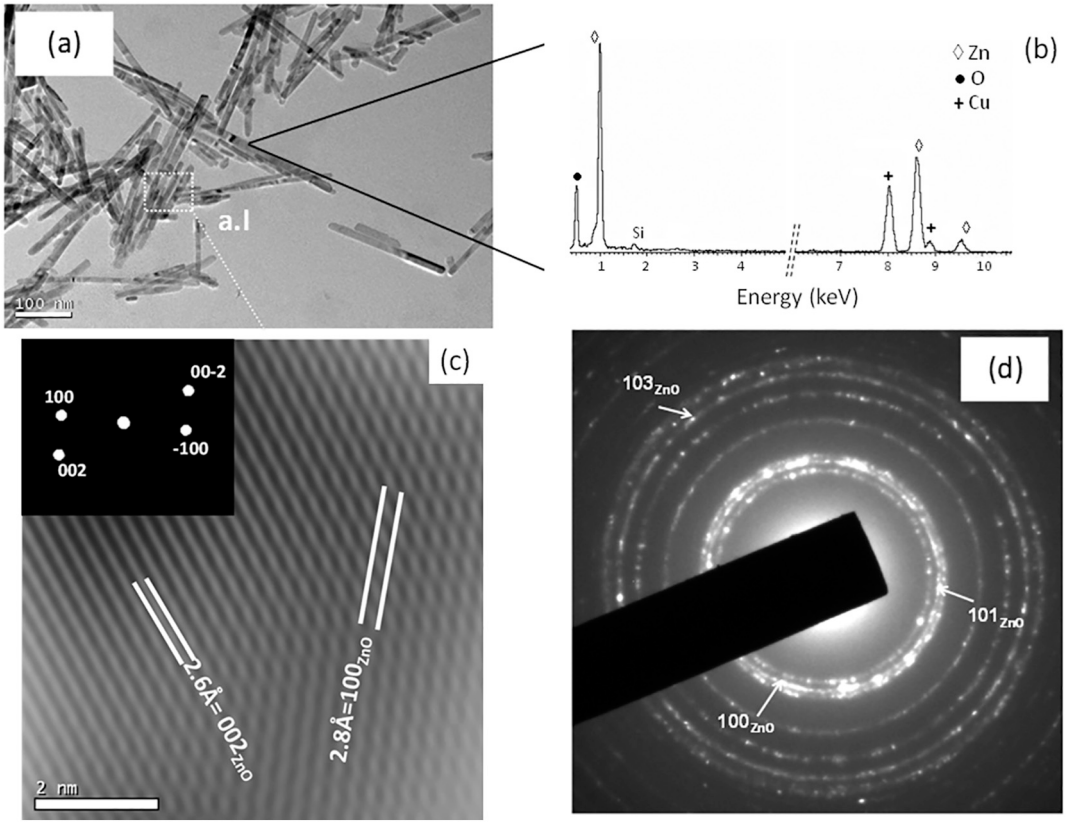

Fig. 3. Low magnification TEM micrograph (bright field mode) (a), EDS spectra (b), HRTEM – FFT (inset) (c) and SAED ring pattern (d) of sample I: pure ZnO.

(Fig. 4.b) of sample II, synthesized according to Table 1. Table 3 details particle dimensions and aspect ratio of all samples calculated from lengths (L) and widths (W) obtained from TEM images. Fig. 4a and b show two kinds of morphology, cylindrical and quasi-spherical nanoparticles. The cylindrical NPs correspond to ZnO nanowires, with homogeneous size and a uniform morphology (about 143 ± 22 nm in length and 13 ± 2 nm in width, aspect ratio of about 11 ± 6). The quasi-spherical nanoparticles correspond to metal Ag NPs(diameter, ϕ. about 17 ± 3 nm), which are well-dispersed on ZnO NWs surface with a proper distribution of secondary particles. These morphologies are similar to those obtained by other authors who have researched to achieve nanostructured systems of Ag/ZnO. [42] [62] [63].

The low magnification HRTEM image (Fig. 4.b) corresponds to a cylindrical particle of the ZnO phase, which is in contact with a quasi-spherical particle of silver. In the Ag Np is visible the development of moiré fringes, suggesting the internal displacement of Ag planes due to lattice defects.

Fig. 4.c displays EDS spectra carried out in different areas of sample II. Results depicted in Fig. 4.c.1 verify that the chemical composition is mainly silver, which belongs to the spherical NPs. However, there is also evidence of Zn and O signals from ZnO NWs on which silver NPs are dispersed. EDS analysis results, shown in Fig. 4.c.2, confirm the presence of ZnO (owing to Zn and O signals) in the nanowires observed in the micrographs. Moreover, there is a small amount of Ag in the study area due to spherical NPs located on the surface of ZnO NWs. This result corresponds to the data obtained by XRD (Fig. 2.II).

The SAED pattern (Fig. 4.d) obtained for the Ag/ZnO sample II confirms the presence of silver on the ZnO NWs surface. As it is evident by this technique, the Ag nano-spheres have a polycrystalline structure. The indexed diffraction rings correspond to (111), (200), (220) and (311) atomic planes of the face-centered-cubic (FCC) structure of Ag (JCPDS card no.: 87-0720). Besides, the ZnO phase is identified by the presence of the (101), (002), (110) and (102) planes (JCPDS card no.: 89-1397). These measurements also confirm the previous XRD results (Fig. 1.II).

While the SAED pattern observed for sample I (Fig. 3.d) suggests its polycrystalline nature with structural defects due to the aggregation of fine wires, the polycrystalline nature of the pattern for sample II (Fig. 4.d) may be caused for overlapping of the Ag spherical NPs and the ZnO nanowires.

From the observations of HRTEM, it is possible to identify particular characteristics inherent to the lattice at the atomic scale. The atomic lattice of the ZnO NWs (Fig. 5a) presents low defect density being possible to observe the growth direction along the plane {002}. The corresponding FFT, oriented along the [010] shows a high intensity in {002} planes (Fig. 5b). Besides, depending on the crystal orientation can be observed a periodicity corresponding to the {100} planes perpendicularly oriented to the growth direction (Fig. 5c) as confirms the FFT (Fig. 5d). The incorporation of silver NPs does not affect the ZnO NWs.

In the case of sample II, specific details can be observed regarding the metal Ag NPs. The nearly circular appearance has a diameter of around 29 to 37 nm. The crystals present their faces affected by twins. Depending on the crystalline face, it is possible to identify single or multiple twinning with parallel lamellae. The twinning also conditions the atomic disorder degree.

Fig. 6 shows silver NPs with different twinning in each face The faces 2 and 3 exhibit the {111} planes as confirming the FFT (Figs. 6c and 7d, respectively). Multiple twins are affecting the face 3. A close-up view of the twinning boundary of region 1 shows multiple twins (Fig. 6b). In this case, three sequences with a spacing of 2.35 Å (111) are delimiting the twin boundary. Partial dislocations (marked with arrows) are affecting the neighboring (111) planes.

In other cases, as shown in Fig. 7, a particle with truncated-octahedron cubic shape (Fig. 7b) shows apparent differences in the disorder degree associated with the {111} twining. Different orientation in the diffuse streaking observed in the FFTs (faces 2 and 3) is due to

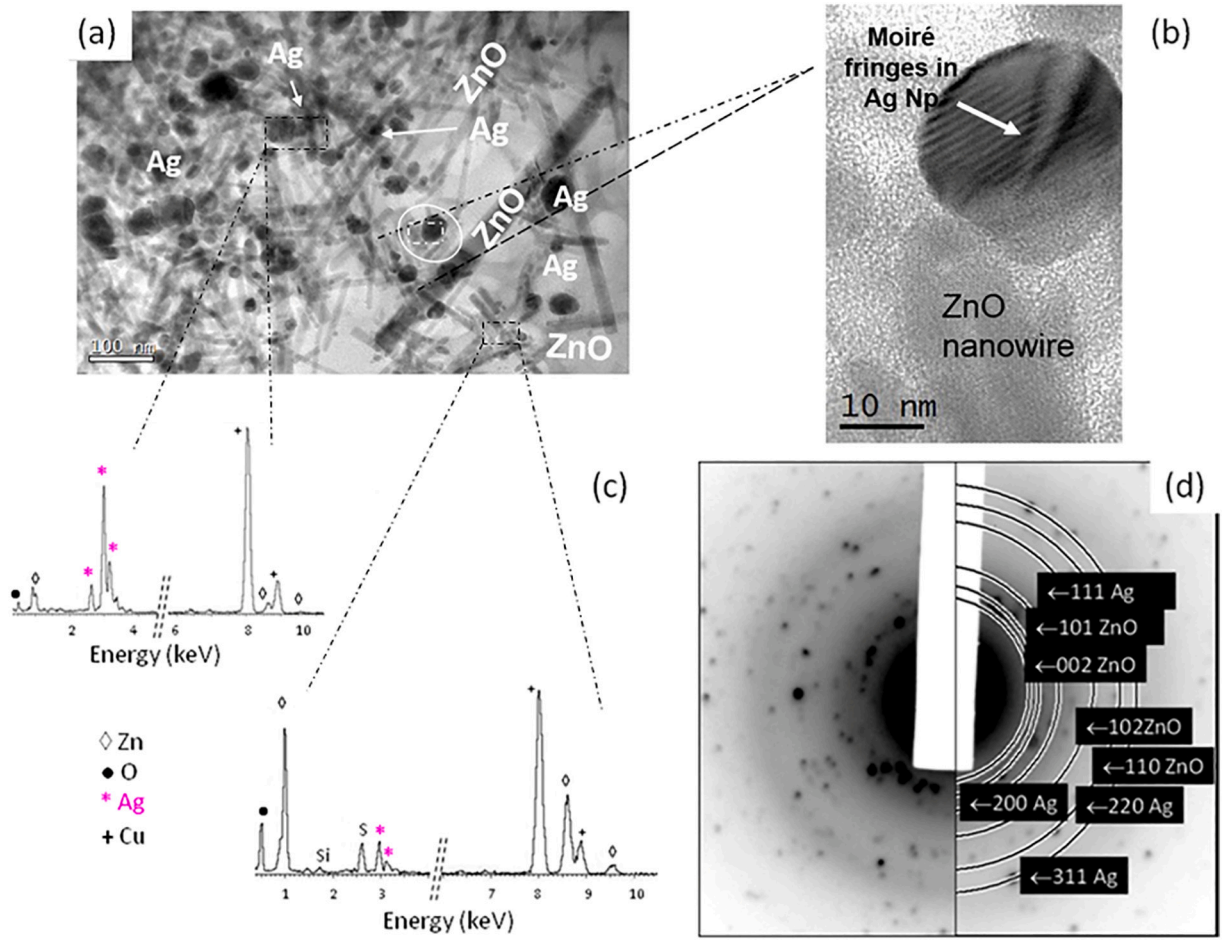

Fig. 4. Low magnification TEM micrograph (bright field mode) with details of silver particles orientation (a), an enlargement shows an HRTEM image of an Ag quasi-spherical NP and a ZnO NW (b), EDS spectra (c) and SAED ring pattern (d) of sample II: Ag/ZnO synthesized nanostructures.

Table 3
Particle dimensions of samples determined from TEM.

Sample	Particle size* (nm)			
	ZnO			Ag
	L	W	AR**	(φ)
I	**65.5 ± 9.7** 138.4 ± 23.9	11.1 ± 2.0	**5.9 ± 1.9** 12.5 ± 4.4	–
II	143.4 ± 22.1	12.6 ± 4.1	11.4 ± 5.5	17.3 ± 3.3
III	**83.1 ± 9.2** 183.6 ± 27.2	12.5 ± 3.8	**6.6 ± 2.8** 14.7 ± 6.6	94.3 ± 29.5
IV	125.4 ± 0.7	14.8 ± 2.5	8.5 ± 1.5	113.1 ± 30.4

In **bold** appear the most representative values of each case.
* Results determined from TEM images.
** Aspect Ratio (AR): Results obtained from length and width (AR = L/W).

shape effects (Figs. 7a and 8c). The FFT corresponding to face 4 shows the crystallographic arrangement along the [011] orientation, where intensity spots corresponding to {111} and {200} suggest minor disorder degree (Fig. 7d). A close-up view of the twinning boundary of region 1 (Fig. 7e) shows parallel-twin lamellae affected by deformation where partial dislocations and stacking faults are affecting the sequence. The arrows indicate local punctual defects.

From the information of HRTEM, it can be deduced that the incorporation of spherical silver NPs on the ZnO NWs could play an essential role in the photocatalytic response. A critical aspect is a role played by point and extended defects The initially formed ZnO NWs consist of very ordered atomic lattices. It is evident that the twinned silver nanocrystals have a high content of defects, where differences in their content depend on the crystalline faces. Indeed, the twining can be subjected to local deformation processes increasing even the density of disorder degree.

Lai et al. [64] suggested that the successful solvothermal method is due to the weak reducing effect of ethanol used as a solvent to obtain metallic silver NPs from Ag^+. In all cases where $AgNO_3$ was added, even in the absence of CTAB, the presence of ethanol leads to the growth of the quasi-spherical metallic silver Nps on the ZnO NWs surface, proving equal results of Y. Zheng et al. [65].

Usually, when sodium hydroxide is present in zinc (2+) solution, the chemical reactions which take place are [66]:

$$Zn^{2+} + 4OH^- \rightarrow Zn(OH)_4^{2-} \quad (1)$$

$$Zn(OH)_4^{2-} \leftrightarrow ZnO + H_2O + 2OH^- \quad (2)$$

In the case where silver ions are also a part of the precursor solution, the following chemical reactions are included in the process [58–60,64–66]:

$$Ag^+ + 2OH^- \rightarrow Ag(OH)_2^- \quad (3)$$

$$Zn(OH)_4^{2-} + 2Ag(OH)_2^- \leftrightarrow Ag_2O/ZnO + 4OH^- \quad (4)$$

In the present work, the molar ratios of OH^-/Zn^{2+} were 10:1 (samples I–III) and 20:1 (sample IV). In these high basic conditions, the ZnO phase is complicated to obtain at RT because the reaction (Eq. 2) is a chemical equilibrium that is easily shifted to the left [64] when a high OH^- concentration exists. However, there are lots of studies demonstrating that in extreme conditions (high temperature and pressure),

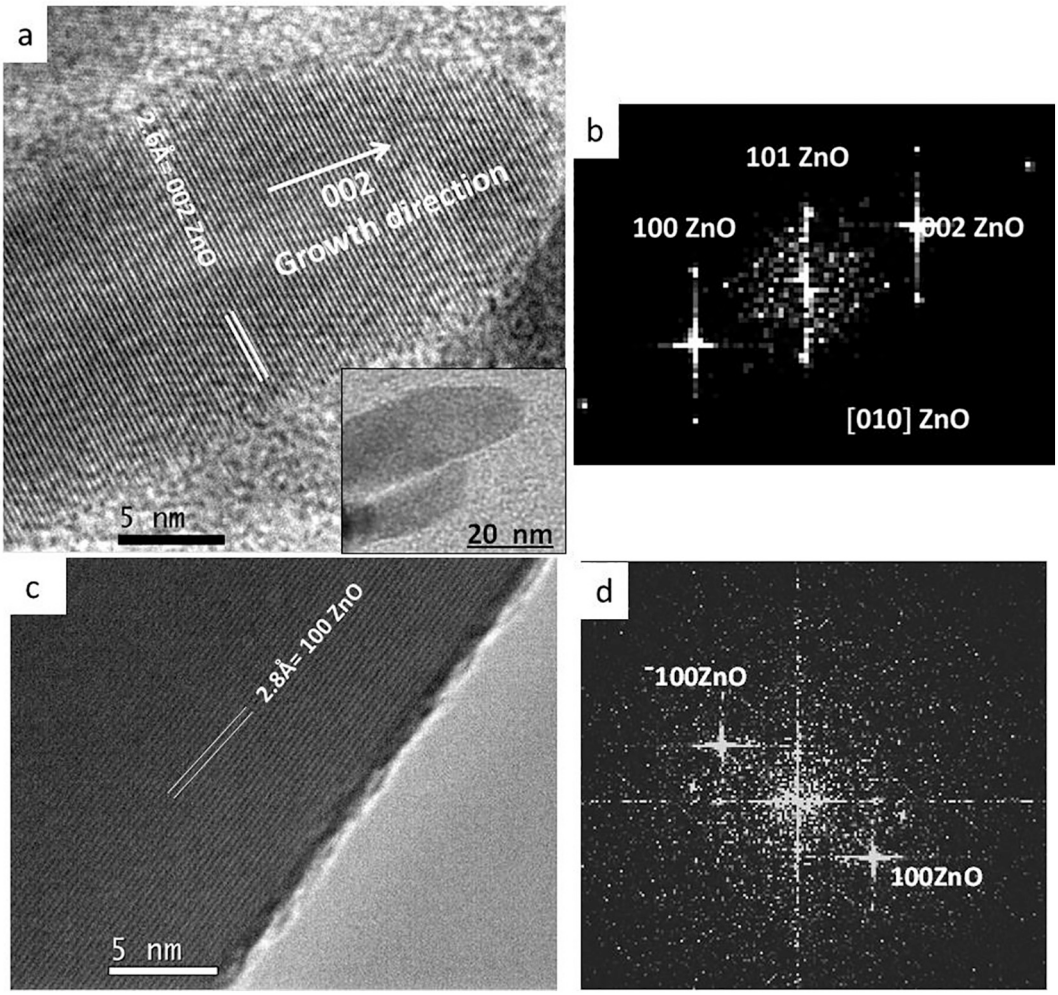

Fig. 5. HRTEM images of ZnO NWs of Sample II: a particular NW showing lattice planes with a distance of 002 indicating the growth direction (a). The corresponding low magnification image is shown as an insert. FFT oriented along the [010] zone axis (b). Detail showing the 100 planes perpendicular to growth direction to ZnO NWs (c). The corresponding FFT confirms the 100 intensity spots (d).

ethanol acts as a weak reducing agent [42,64,65]. Therefore, in our solvothermal process, ethanol could deprive the oxygen ions presented on the ZnO surface, creating oxygen vacancy ($V_o^{\bullet\bullet}$) on the surface of ZnO NWs (Eq. 2 or Eq. 3). Moreover, in these conditions, the reduction reaction of Ag_2O would be favored, leading to the formation of pure metallic Ag NPs on the surface of ZnO NWs (eq. 3).

$$ZnO \xrightarrow{solvothermal} ZnO_x(1-X)V_0^{\bullet\bullet}, 0 < X < 1 \quad (5)$$

$$Ag_2O/ZnO \xrightarrow{solvothermal} Ag/ZnO_x(1-X)V_0^{\bullet\bullet}, 0 < X < 1 \quad (6)$$

3.4. Optical properties. UV–vis diffuse reflectance spectroscopy (DRS, GAP values determination)

The energy bandgap value was estimated by extrapolation of the linear portion of the graph, between the modified Kubelka-Munk function [F(R)·hν]2 versus photon energy (hν), where, h is the Planck's constant and ν is the frequency of light, as reported in previous work [67]. Table 4 shows the samples' extrapolated value of the energy bandgap (Eg). Compared with bulk ZnO (3.37 eV), the Eg reduced to 3.21 eV when it reached the nanoscale, as observed in the pure ZnO NWs (sample I). This value is not more distant from the bandgap of commercial ZnO nanoparticles (3.18 eV) [68]. Observing samples II–VI, silver NPs does not substantially affect the Eg values remaining almost constant (3.23–2.29 eV), compared with pure ZnO NWs (3.21 eV). However, the Eg of sample III is slightly higher than sample II (3.24 and 3.29 eV, respectively), showing that GAP is minimally increased with reaction time. This decrease could be due to the bandgap energy, which is directly related to the particle size of the samples and the defect presence of Ag/ZnO.

3.5. Measurement of surface area (N_2 gas adsorption/desorption, BET values estimation)

Table 4 summarizes the specific surface area values. Values are between 25 and 59 m^2/g, higher than those reported commercial ZnO NPs, around 9.8 m^2/g [70]. These values may be due to the size of NWs. Moreover, these values are in the range commonly accepted for mesoporous materials (according to the IUPAC classification, S_{BET} = 10–200 m^2/g). However, BET values show a slight reduction in the presence of silver Nps, which could be due to the silver NPs deposition on the ZnO NWs, which reduces the available ZnO surface. The lowest specific surface area corresponds to sample IV, which has a high level of agglomeration, as observed in the SEM images.

3.6. Inductively coupled plasma-atomic emission spectroscopy (ICP-AES)

Comparing BET and elemental composition of samples (Table 4.) indicates how higher metal loadings coincide with larger BET areas, and consequently, there is more surface area to deposit the silver. Besides,

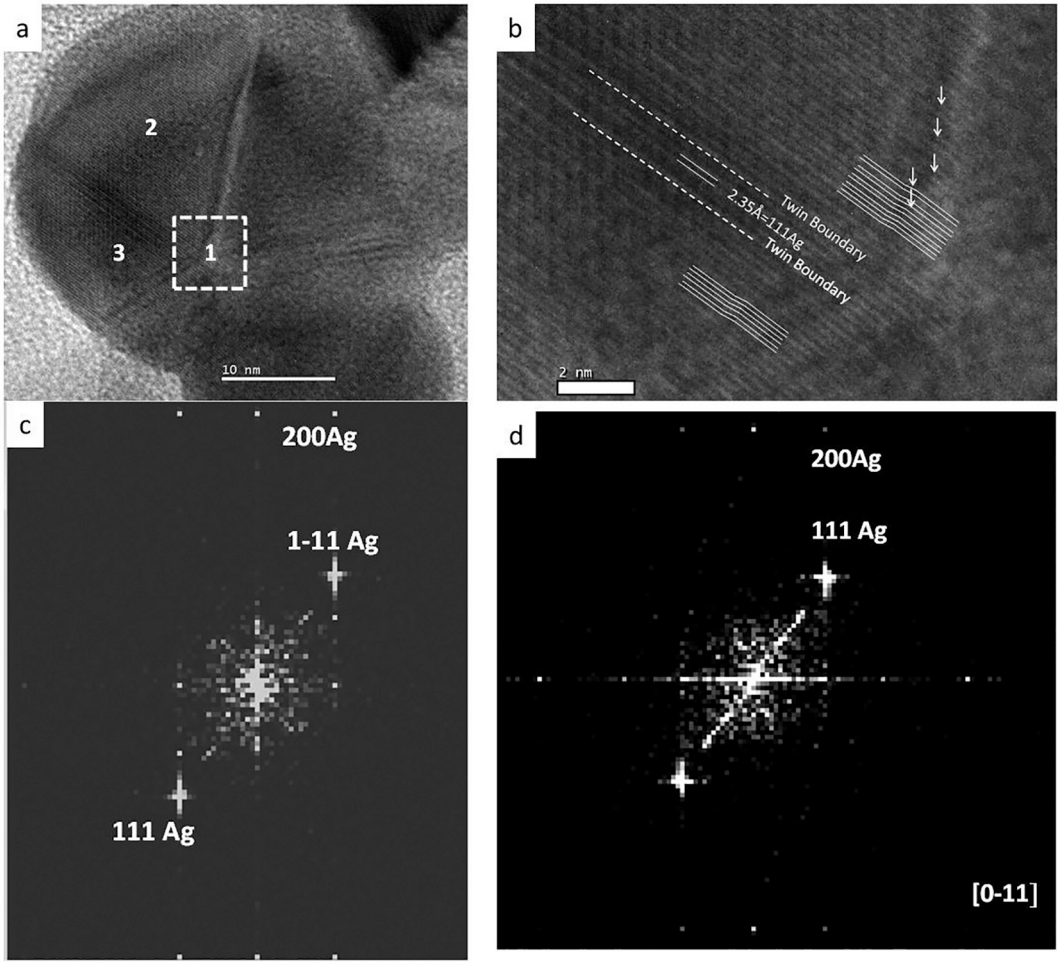

Fig. 6. HRTEM image of silver NPs corresponding to sample II (a). A close-up of the region (marked as 1) shows local details of the twin boundaries and partial dislocations associated with twin sequences (b). FFT showing the 111 and 200 of silver NP (c). Diffuse streaking corresponds to the region affected by dislocations and faults of figure b (d).

sample IV has the lowest silver load, which could be due to higher zinc precursor concentration and major particle agglomeration.

3.7. Photocatalysis

Fig. 8 shows the MB degradation percentage with the irradiation time. According to previous works, if there are no ZnO nanostructures in media, no significant MB degradation occurs under irradiation with UV light [29,49]. Therefore, for interpreting the results of Fig. 5, it is necessary to discuss them individually, according to different synthesis conditions.

The precursor concentration indicates that a lower Ag^{+}/Zn^{2+} molar ratio causes a lower percentage of silver available and, therefore, worse catalytic results. Furthermore, sample IV was synthesized without dispersant and at a long reaction time (18 h).

The reaction time shows that samples prepared at a longer time (samples III and IV) present worse photocatalytic behavior due to further growth of the particles. Longer reaction time leads to higher inhomogeneity in the samples' sizes, aspect ratios, and a higher aggregation observed (Fig. 2.e).

Apart from synthesis conditions, the dispersant also plays a vital role in changing the morphology of ZnO nanostructures [48]. Studies carried out in zinc oxide by Brunauer-Emmett-Teller (BET) Surface Area Analysis [17,71] demonstrate that the available surface area of nanostructures affects the catalytic results. The morphology and size that determine the surface area are critical parameters in photocatalytic activity [47]. As displayed in Fig. 8, samples synthesized with CTAB (samples II and III) have the best catalytic behavior. Due to the synergic effect of dispersant and solvent, the dispersant can interact with growth units of ZnO to generate active sites on the surface of ZnO nuclei so that ZnO NWs are created from those sites [4,51–53]. Therefore, it leads to a larger surface area than samples synthesized without CTAB (samples I and IV).

When the Ag precursor is added in the presence of CTAB, and more considerable reaction time (sample III), its photocatalytic activity is almost similar to that of pure ZnO (sample I). In this case, it is necessary to consider that sample III is less homogenous than the sample I despite having silver (Fig. 2).

Compared with pure ZnO (sample I), loading an amount of Ag on ZnO NWs was expected to enhance its photocatalytic activity. However, as shown in Fig. 8, sample IV synthesized with Ag exhibits worse photocatalytic activity than the sample I (pure ZnO). This result is justified with particle sizes (Table 3). In this Table 3, sample I presents a lower aspect ratio (5.9 ± 1.9) than sample IV (8.5 ± 1.5), and the particle size of Ag nano-spheres in the second one is the largest obtained (113.1 ± 30.4 nm). This could decrease the available surface area due to nanoparticles agglomeration caused by their growth. Studies carried out by W.L. Ong et al. [72] on various heterostructured ZnO-Pt/Ag/CuO nanowires showed that the high agglomeration of the NPs could reduce the surface area available for photoreactivity.

Analyzing samples II and III, both synthesized in the presence of CTAB. The first one shows better catalytic activity. It could be related to

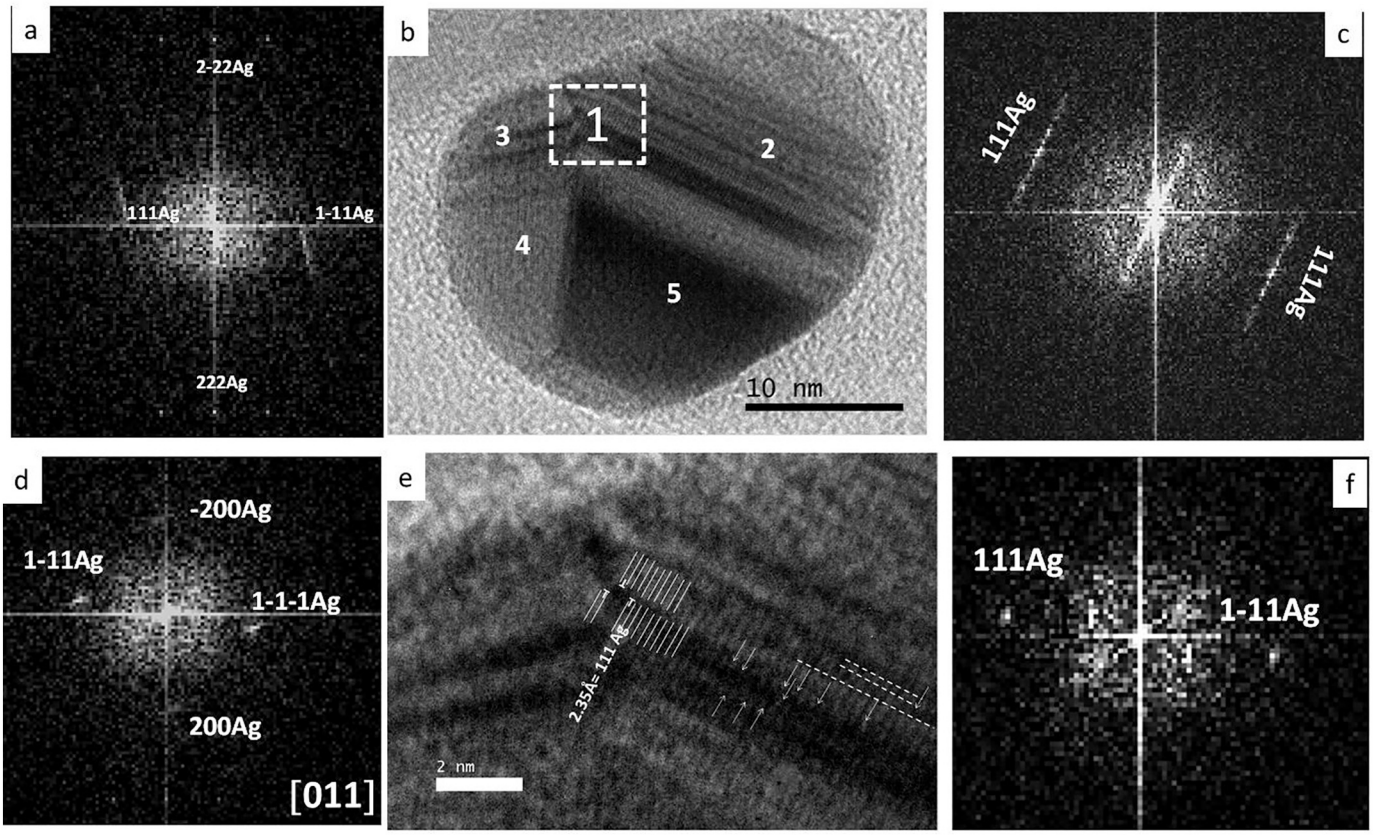

Fig. 7. HRTEM images of a partially deformed silver nanoparticle with multiple twining on {111} corresponding to sample II (b). Different orientations of each face are confirmed in the FFT patterns (a, c, d, and f). For more details, see the text. Enlarged image showing the stacking faults and partial dislocations of region 1 (e).

the surface and the particle size effects. i) Sample III has a heterogeneous morphology with a worse silver Nps dispersion (see SEM images, Fig. 2). ii) The particle size of sample III presents two ZnO NWs` value distributions (length 83.1 ± 9.2 and 183.6 ± 27.2 nm). Therefore, sample II shows a narrow size distribution leading to the optimum aspect ratio of about 11, which may be related to the available surface area. Besides, the particle diameters of the silver obtained in sample III (94.3 ± 29.5 nm) are much higher than in sample II (17.3 ± 3.3 nm), which can cause problems in dispersion and a decrease in the available amount of silver to collect the electrons from CB of irradiated ZnO NWs. Thus, the effect of size on the PCA could be due to the particle size. If the particle size decreases, the number of dispersed particles per volume in the solution increases. It will conduce to an enhancement of the photon absorbance. Besides, if BET values of the ZnO nanowires decrease, it will promote the adsorption of more dye molecules. Therefore, the deviation in PCA should also arise from a morphology difference. These results agree with the work performed by Y. Zheng et al. [65], verifying that the photocatalytic activity of Ag/ZnO photocatalysts depends on mainly of the dispersion of Ag nanoparticles on ZnO NWs surface. Therefore, the higher the dispersity of Ag nanoparticles onto ZnO NWs, the higher the photocatalytic activity of Ag/ZnO photocatalyst. Moreover, the dispersity of nanostructured systems of Ag/ZnO is another critical factor for liquid-phase photocatalysis due to the UV-light efficiency.

In all cases, MB degradation was higher than 64% after two hours of exposure. Also, increasing the time up to 120 min. (from 60 min.), the percentage of MB degradation increases. So that, with more irradiation time, the number of photons absorbed increases, producing more OH– by facilitating the oxidation of MB. Sample II, synthesized at 120°C and intermediate reaction time (6 h), showed the best results of MB degradation (higher than 99%) with a high Ag^{+}/Zn^{2+} ratio in the presence of CTAB. It confirms that the CTAB affects the system's morphology, one of the most significant parameters, even if it is more critical than the presence or absence of silver. The results of the photocatalytic study confirmed the viability of the prepared systems for their application in the removal of organic dyes in water.

Furthermore, these results showed that photocatalytic activity could be improved by incorporating silver nanoparticles on zinc oxide NWs. Thus, the superior photocatalytic performance of nanostructured systems of Ag/ZnO (samples II–IV) can be explained by the fact that coupling of Ag with ZnO leads to a larger surface area (compared with pure ZnO), which gives rise to an enhancing of the adsorption capacity of pollutants. Besides, the combination of ZnO and Ag can increase the separation efficiency of photogenerated carriers and improve their photo-stability of ZnO [17,18,20,32,73] [74]. Therefore, given that the energy level of the conduction band of ZnO is higher than the Fermi level of Ag/ZnO structure, electrons flow from ZnO nanostructures to Ag nanoparticles. So, Ag NPs perform the role of photogenerated electrons sink very efficiently, therefore, the recombination of electrons and holes could be inhibited [8].

Fig. 8.c depicts Ln (C_t/C_0) plotted data versus photodegradation time, where C_0 and C_t represent the concentration of aqueous MB at the initial and after a given reaction time, respectively. In this plot, the MB degradation reaction can be modeled as a pseudo-first-order reaction obtaining from the slope of the linear extrapolations the experimental constant, K_{exp} (Fig. 8.c).. Moreover, the elimination half-life, $t_{1/2}$, is calculated from the following equation:

$$t_{1/2} = \left(\frac{1}{k_{exp}}\right) \cdot \mathrm{Ln}2 \tag{7}$$

Synthesized samples' experimental kinetic parameters are shown in Table 5. The rate of empirical constants follows the sequence: sample II > III > I > IV; these values are in the same tendency that % efficiency of elimination results. The highest reaction rate experimental constant,

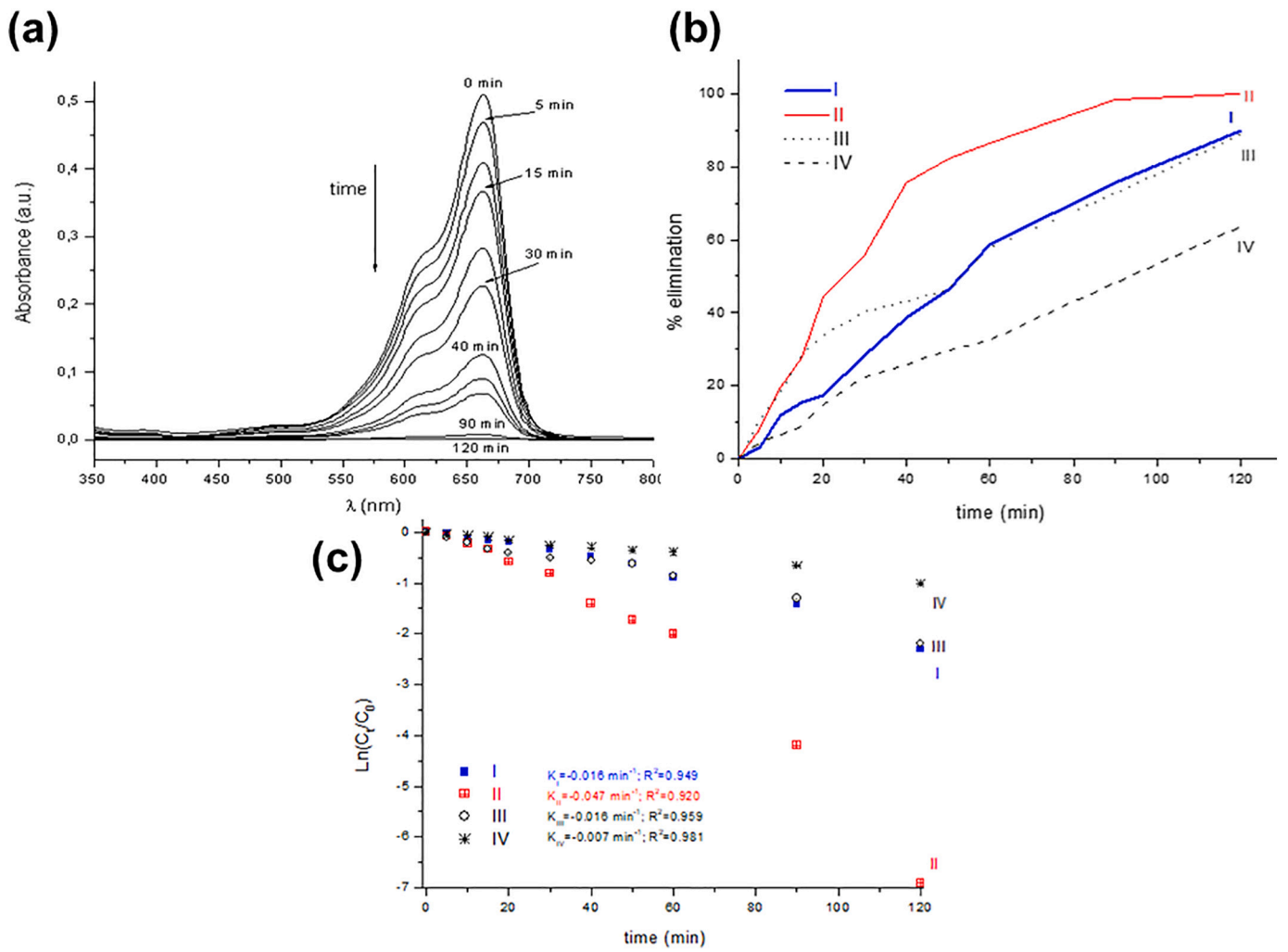

Fig. 8. UV–visible absorption spectra of MB dye decomposition by sample II (a) and degradation percentage of MB in all synthesized samples (b) during exposure to UV light. The plotted data of Ln (Ct/C0) versus photodegradation time (c). * Results obtained by % degradation = (C0-Ct)·100/C0, where C0 is the concentration of MB solution before photocatalytic reaction, and Ct is a concentration of MB solution with photocatalyst following UV light exposure for time "t".

Table 4
Band GAP values, BET surface areas and composition (wt%) of synthesized samples.***

Sample	Band GAP* (eV)	BET surface** ($m^2 \cdot g^{-1}$)	% w/w (Zn)***	% w/w (Ag)***
I	3.21	59.3	21	0
II	3.24	42.6	60	17
III	3.29	41.4	57	18
IV	3.23	24.7	63	7

*Band GAP calculated from the Kubelka-Munk transformed reflectance spectra of synthesized samples.
Theoretical Eg = 3.37 eV.
**BET surface area calculated from the linear part of the BET plot (P/P0 = 0.05–0.3).
Theoretical: BET <10 m^2/g (NWs φ < 200 nm) [69].
*** %w/w estimated by ICP analysis.

$3.2 \cdot 10^{-2}$ min^{-1}, is presented for sample II, which achieves the 50% elimination after only 22 min of irradiation.

The chemical mechanism that leads to organic pollutant degradation is proposed in Fig. 9, being in good agreement with other authors [72,75] where: VB and CB are the valence and conduction bands, respectively.

Table 5
Experimental kinetic parameters of the synthesized samples.

Sample	% elimination (after 2 h)	$k_{exp.}$ (min^{-1})	$t_{1/2}$ (min)
I	90.1	0.013	53
II	99.9	0.032	22
III	88.9	0.014	50
IV	63.7	0.007	99

$$ZnO \xrightarrow{h\gamma} h^+ (VB) + e^- (CB) \text{“electron} - \text{hole”pair} \quad (8)$$

$$OH^{\bullet -} + organic\ dye \rightarrow CO_2 + H_2O \quad (9)$$

$$O_2^{\bullet -} + organic\ dye \rightarrow CO_2 + H_2O \quad (10)$$

The nanoscale observation of the ZnO nanowires indicated a highly ordered surface. In contrast, silver nanoparticles exhibited a high disorder degree, and their inclusion improved photocatalytic effectiveness. The higher content of nanoscale defects coincided with the sample that gave better photocatalytic efficiency (Ag^+/Zn^{2+} (0.2/1) molar ratio). The presence of twinning-type defects, local stacking faults, and dislocations reduced the recombination reaction favoring photocatalysis. Previous works have reported how the formation and growth of twins result in substantial evolution of microstructures and properties in a

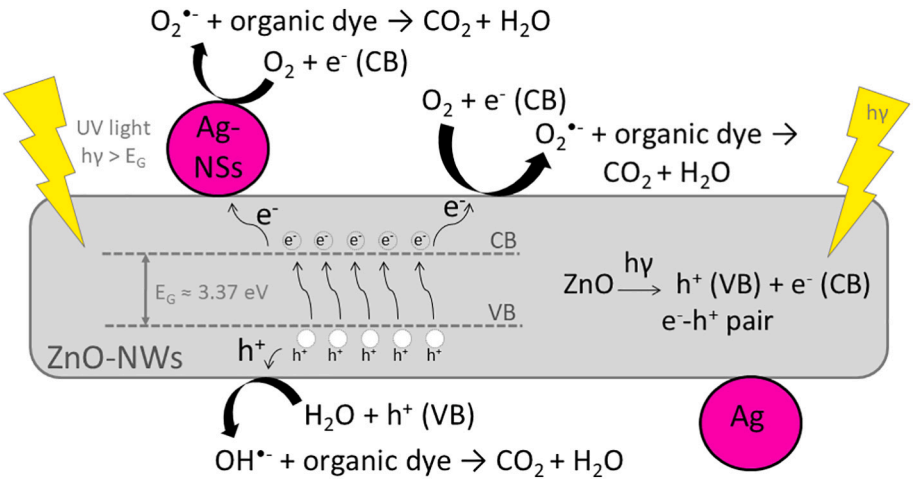

Fig. 9. The proposed chemical mechanism for degrading of organic pollutants.

large variety of metallic materials [76]. Besides, catalytic studies have pointed out the importance of surface defects in the effectiveness of catalysis [77].

4. Conclusions

The present research got successfully synthesized Ag/ZnO-based nanostructures with aspect ratios ranging from 5.9 to 11.4; obtaining ZnO nanowires with hexagonal wurtzite structure and nanoparticles of Ag with Ag face-centered-cubic (FCC) structure. XRD has shown no evidence of the existence of silver in interstitial or substitutional positions in the host structure of ZnO and secondary phases. Metallic silver formed spherical nanoparticles distributed onto the nanowires of ZnO. By HRTEM, the presence of twinned silver nanocrystals with a high degree of disorder at the atomic level (stacking faults, dislocations) and differences depending on the crystalline faces could play an essential role in the photocatalytic response. The application of CTAB as a dispersant in the synthesis of Ag/ZnO composites strongly affects the particles' nucleation and growth, affecting the final morphology of nanostructures and the dispersion thereof. The photocatalytic behavior improved by incorporating silver nanoparticles on nanowires of ZnO. Furthermore, results close to 100% degradation were obtained for a sample synthesized at intermediate reaction time, high Ag^+/Zn^{2+} ratio, and in the presence of a dispersant, demonstrating that these were the optimal operating conditions. Therefore, the Ag/ZnO-based nanostructures PCA depends upon the crystallinity, surface area, and particle morphology, which also rely highly on the synthesis conditions.

Data availability

The raw/processed data required to reproduce these findings cannot be shared at this time as the data also forms part of an ongoing study.

Declaration of Competing Interest

The authors declare that they have no known competing financial interests or personal relationships that could have appeared to influence the work reported in this paper.

Acknowledgments

This work has been supported by the Innovation and Education Ministry (ref. MAT2013-47460-C5-5-P and MAT2016-80875-C3-3-R), the Autonomous Region Program of Madrid (ref. S2018/NMT-4411 and S2013/MIT-2862), the Geomateriales 2 program (S2013/MIT_2914), the TOP Heritage (P2018/NMT-4372) of the Community of Madrid, the Innovation and Education Ministry (MAT201347460-C5-5-P) and the Ministry of Education, Science and Technological Development of Serbia (projects No. 172035 and 45020). Besides, we would like to thank the Master of "Materials Science" of Carlos III University (Spain) for providing financial and laboratory equipment support.

References

[1] J. Cai, J. Huang, S. Wang, J. Iocozzia, Z. Sun, J. Sun, Y. Yang, Y. Lai, Z. Lin, Crafting mussel-inspired metal nanoparticle-decorated ultrathin graphitic carbon nitride for the degradation of chemical pollutants and production of chemical resources, Adv. Mater. 31 (2019) 1–11, https://doi.org/10.1002/adma.201806314.
[2] H. Saleem, S.J. Zaidi, Developments in the application of nanomaterials for water treatment and their impact on the environment, Nanomaterials 10 (2020) 1794, https://doi.org/10.3390/nano10091764.
[3] S. Atalay, G. Ersöz, Review on catalysis in advanced oxidation processes, in: Nov. Catal. Adv. Oxid. Org. Pollut., Springer, 2016, pp. 35–58, https://doi.org/10.1007/978-3-319-28950-2.
[4] C. Santhosh, V. Velmurugan, G. Jacob, S.K. Jeong, A.N. Grace, A. Bhatnagar, Role of nanomaterials in water treatment applications: a review, Chem. Eng. J. 306 (2016) 1116–1137, https://doi.org/10.1016/j.cej.2016.08.053.
[5] X. Wang, H. Tian, Y. Yang, H. Wang, S. Wang, W. Zheng, Y. Liu, Reduced graphene oxide/CdS for efficiently photocatalystic degradation of methylene blue, J. Alloys Compd. 524 (2012) 5–12, https://doi.org/10.1016/j.jallcom.2012.02.058.
[6] S. Garcia-Segura, E. Brillas, Applied photoelectrocatalysis on the degradation of organic pollutants in wastewaters, J. Photochem. Photobiol. C Photochem. Rev. 31 (2017) 1–35, https://doi.org/10.1016/j.jphotochemrev.2017.01.005.
[7] M. Ge, C. Cao, J. Huang, S. Li, Z. Chen, K.Q. Zhang, S.S. Al-Deyab, Y. Lai, A review of one-dimensional TiO2 nanostructured materials for environmental and energy applications, J. Mater. Chem. A 4 (2016) 6772–6801, https://doi.org/10.1039/c5ta09323f.
[8] Y.F. Lin, J.L. Chen, K.S. Chang, K.L. Tung, Insight into the roles of ethylenediamine and hydrazine for the synthesis of ZnO micro/nanostructures using solvothermal process, J. Nanopart. Res. 15 (2013), https://doi.org/10.1007/s11051-012-1398-z.
[9] T.-D. Nguyen-Phan, V.H. Pham, T.V. Cuong, S.H. Hahn, E.J. Kim, J.S. Chung, S. H. Hur, E.W. Shin, Fabrication of TiO2 nanostructured films by spray deposition with high photocatalytic activity of methylene blue, Mater. Lett. 64 (2010) 1387–1390, https://doi.org/10.1016/j.matlet.2010.03.033.
[10] Y. Zhang, J. Wan, Y. Ke, A novel approach of preparing TiO2 films at low temperature and its application in photocatalytic degradation of methyl orange, J. Hazard. Mater. 177 (2010) 750–754, https://doi.org/10.1016/j.jhazmat.2009.12.095.
[11] M. Kobayashi, W. Kalriess, Photocatalytic activity of titanium dioxide and zinc oxide, Cosmet. Toilet. 112 (1997) 83–85.
[12] Y.K.L.M.Z. Ge, C.-Y.- Cao, S.H. Li, Y.-X. Tang, L.N. Wang, N. Qi, J.-Y. Huang, K. Q. Zhang, S.S. Al-Deyabe, In situ plasmonic Ag nanoparticle anchored TiO2 nanotube arrays as visible-light-driven photocatalysts for enhanced water splitting, Nanoscale 8 (2016) 5226–5234, https://doi.org/10.1039/x0xx00000x.
[13] X. Zhang, M. Ge, J. Dong, J. Huang, J. He, Y. Lai, Polydopamine-inspired design and synthesis of visible-light-driven Ag NPs@C@elongated TiO2 NTs core-shell nanocomposites for sustainable hydrogen generation, ACS Sustain. Chem. Eng. 7 (2019) 558–568, https://doi.org/10.1021/acssuschemeng.8b04088.
[14] S. Akir, A. Barras, Y. Coffinier, M. Bououdina, R. Boukherroub, A.D. Omrani, Eco-friendly synthesis of ZnO nanoparticles with different morphologies and their visible light photocatalytic performance for the degradation of rhodamine B, Ceram. Int. 42 (2016) 10259–10265, https://doi.org/10.1016/j.ceramint.2016.03.153.

[15] Z.C. Feng, Handbook of Zinc Oxide and Related Materials: Volume Two: Devices and Nano-Engineering, CRC Press, 2013, 978-1-4398-5575-1.
[16] A. Moezzi, A.M. McDonagh, M.B. Cortie, Zinc oxide particles: synthesis, properties and applications, Chem. Eng. J. 185–186 (2012) 1–22, https://doi.org/10.1016/j.cej.2012.01.076.
[17] S. Kuriakose, V. Choudhary, B. Satpati, S. Mohapatra, Enhanced Photocatalytic Activity of Ag – ZnO Hybrid Plasmonic Nanostructures Prepared by a Facile Wet Chemical Method, 2014, pp. 639–650, https://doi.org/10.3762/bjnano.5.75.
[18] R. Medhi, M.D. Marquez, T.R. Lee, Visible-light-active doped metal oxide nanoparticles: review of their synthesis, properties, and applications, ACS Appl. Nano Mater. 3 (2020) 6156–6185, https://doi.org/10.1021/acsanm.0c01035.
[19] C. Berberidou, V. Kitsiou, D.A. Lambropoulou, A. Antoniadis, E. Ntonou, G. C. Zalidis, I. Poulios, Evaluation of an alternative method for wastewater treatment containing pesticides using solar photocatalytic oxidation and constructed wetlands, J. Environ. Manag. 195 (2017) 133–139, https://doi.org/10.1016/j.jenvman.2016.06.010.
[20] R.S. Varma, N. Thorat, R. Fernandes, D.C. Kothari, N. Patel, A. Miotello, Dependence of photocatalysis on charge carrier separation in Ag-doped and decorated TiO2 nanocomposites, Catal. Sci. Technol. 6 (2016) 8428–8440, https://doi.org/10.1039/c6cy01605g.
[21] N. Tamaekong, C. Liewhiran, A. Wisitsoraat, S. Phanichphant, Acetylene sensor based on Pt/ZnO thick films as prepared by flame spray pyrolysis, Sensors Actuators B Chem. 152 (2011) 155–161, https://doi.org/10.1016/j.snb.2010.11.058.
[22] A. Šutka, T. Käämbre, R. Pärna, I. Juhnevica, M. Maiorov, U. Joost, V. Kisand, Co doped ZnO nanowires as visible light photocatalysts, Solid State Sci. 56 (2016) 54–62, https://doi.org/10.1016/S0167-2738(01)00888-8.
[23] C.B. Ong, L.Y. Ng, A.W. Mohammad, A review of ZnO nanoparticles as solar photocatalysts: synthesis, mechanisms and applications, Renew. Sust. Energ. Rev. 81 (2018) 536–551, https://doi.org/10.1016/j.rser.2017.08.020.
[24] W. Ben Haj Othmen, M. Ben Ali, W. Bouslama, H. Elhouichet, Solar driven photocatalytic properties of Sm3+ doped ZnO nanocrystals, Ceram. Int. 46 (2020) 18878–18887, https://doi.org/10.1016/j.ceramint.2020.04.208.
[25] N. Sinha, G. Ray, S. Bhandari, S. Godara, B. Kumar, Synthesis and enhanced properties of cerium doped ZnO nanorods, Ceram. Int. 40 (2014) 12337–12342, https://doi.org/10.1016/j.ceramint.2014.04.079.
[26] R. Zamiri, A.F. Lemos, A. Reblo, H.A. Ahangar, J.M.F. Ferreira, Effects of rare-earth (Er, la and Yb) doping on morphology and structure properties of ZnO nanostructures prepared by wet chemical method, Ceram. Int. 40 (2014), https://doi.org/10.1016/j.ceramint.2013.06.034.
[27] P. Pascariu, C. Cojocaru, N. Olaru, P. Samoila, A. Airinei, M. Ignat, L. Sacarescu, D. Timpu, Novel rare earth (RE-La, Er, Sm) metal doped ZnO photocatalysts for degradation of congo-red dye: synthesis, characterization and kinetic studies, J. Environ. Manag. 239 (2019) 225–234, https://doi.org/10.1016/j.jenvman.2019.03.060.
[28] J. Liqiang, W. Baiqi, X. Baifu, L. Shudan, S. Keying, C. Weimin, F. Honggang, Investigations on the surface modification of ZnO nanoparticle photocatalyst by depositing Pd, J. Solid State Chem. 177 (2004) 4221–4227, https://doi.org/10.1016/j.jssc.2004.08.016.
[29] G. Kenanakis, N. Katsarakis, E. Koudoumas, Influence of precursor type, deposition time and doping concentration on the morphological, electrical and optical properties of ZnO and ZnO:Al thin films grown by ultrasonic spray pyrolysis, Thin Solid Films 555 (2014) 62–67, https://doi.org/10.1016/j.tsf.2013.10.015.
[30] K. Jayanthi, S. Chawla, K.N. Sood, M. Chhibara, S. Singh, Dopant induced morphology changes in ZnO nanocrystals, Appl. Surf. Sci. 255 (2009) 5869–5875, https://doi.org/10.1016/j.apsusc.2009.01.032.
[31] M. Checa, F. Auneau, J. Hidalgo-Carrillo, A. Marinas, J.M. Marinas, C. Pinel, F. J. Urbano, Catalytic transformation of glycerol on several metal systems supported on ZnO, Catal. Today 196 (2012) 91–100, https://doi.org/10.1016/j.cattod.2012.02.036.
[32] V. Montes, M. Checa, A. Marinas, M. Boutonnet, J.M. Marinas, F.J. Urbano, S. Järas, C. Pinel, Synthesis of different ZnO-supported metal systems through microemulsion technique and application to catalytic transformation of glycerol to acetol and 1,2-propanediol, Catal. Today 223 (2014) 129–137, https://doi.org/10.1016/j.cattod.2013.09.021.
[33] Q. Deng, X. Duan, D.H.L. Ng, H. Tang, Y. Yang, M. Kong, Z. Wu, W. Cai, G. Wang, Ag nanoparticle decorated nanoporous ZnO microrods and their enhanced photocatalytic activities, ACS Appl. Mater. Interfaces 4 (2012) 6030–6037, https://doi.org/10.1021/am301682g.
[34] W. Hu, Q. Zhang, K. Luo, H. Yuan, J. Li, M. Xu, S. Xu, Enhanced photocatalytic properties of CuO–ZnO nanocomposites by decoration with Ag nanoparticles, Ceram. Int. 46 (2020) 24753–24757, https://doi.org/10.1016/j.ceramint.2020.06.235.
[35] Y. Zhang, T.R. Nayak, H. Hong, W. Cai, Biomedical applications of zinc oxide nanomaterials, Curr. Mol. Med. 13 (2014) 1633–1645.
[36] S. Hameed, A.T. Khalil, M. Ali, M. Numan, Greener synthesis of ZnO and Ag – ZnO nanoparticles using Silybum marianum for diverse biomedical applications, Nanomedicine 14 (2019) 655–673.
[37] M.A. Kakakhel, F. Wu, J.-D. Gu, H. Feng, K. Shah, W. Wang, Controlling biodeterioration of cultural heritage objects with biocides : a review, Int. Biodeterior. Biodegrad. 143 (2019) 104721, https://doi.org/10.1016/j.ibiod.2019.104721.
[38] S.A. Ruffolo, M. Francesco, L. Russa, Nanostructured coatings for stone protection : an overview, Front. Mater. 6 (2019) 1–8, https://doi.org/10.3389/fmats.2019.00147.
[39] H. Liu, Y. Hu, Z. Zhang, X. Liu, H. Jia, B. Xu, Synthesis of spherical Ag/ZnO heterostructural composites with excellent photocatalytic activity under visible light and UV irradiation, Appl. Surf. Sci. 355 (2015) 644–652, https://doi.org/10.1016/j.apsusc.2015.07.012.
[40] U. Alam, T.A. Shah, A. Khan, M. Muneer, One-pot ultrasonic assisted sol-gel synthesis of spindle-like Nd and V codoped ZnO for efficient photocatalytic degradation of organic pollutants, Sep. Purif. Technol. 212 (2019) 427–437, https://doi.org/10.1016/j.seppur.2018.11.048.
[41] Ö.A. Yıldırım, C. Durucan, Effect of precipitation temperature and organic additives on size and morphology of ZnO nanoparticles, J. Mater. Res. 27 (2012) 1452–1461, https://doi.org/10.1557/jmr.2012.58.
[42] C. Wu, L. Shen, Y. Cai Zhang, Q. Huang, Solvothermal synthesis of Ag/ZnO nanocomposite with enhanced photocatalytic activity, Mater. Lett. 106 (2013) 104–106, https://doi.org/10.1016/j.matlet.2013.05.004.
[43] Y.X. Wang, J. Sun, X. Fan, X. Yu, A CTAB-assisted hydrothermal and solvothermal synthesis of ZnO nanopowders, Ceram. Int. 37 (2011) 3431–3436, https://doi.org/10.1016/j.ceramint.2011.04.134.
[44] A. Kolodziejczak-Radzimska, T. Jesionowski, Zinc oxide-from synthesis to application: a review, Materials (Basel) 7 (2014) 2833–2881, https://doi.org/10.3390/ma7042833.
[45] L. Xu, Y.S. Ding, C.H. Chen, L. Zhao, C. Rimkus, R. Joesten, S.L. Suib, 3D flowerlike α-nickel hydroxide with enhanced electrochemical activity synthesized by microwave-assisted hydrothermal method, Chem. Mater. 20 (2008) 308–316, https://doi.org/10.1021/cm702207w.
[46] N. Talebian, S.M. Amininezhad, M. Doudi, Controllable synthesis of ZnO nanoparticles and their morphology-dependent antibacterial and optical properties, J. Photochem. Photobiol. B Biol. 120 (2013) 66–73, https://doi.org/10.1016/j.jphotobiol.2013.01.004.
[47] A. Kajbafvala, H. Ghorbani, A. Paravar, J.P. Samberg, E. Kajbafvala, S. K. Sadrnezhaad, Effects of morphology on photocatalytic performance of zinc oxide nanostructures synthesized by rapid microwave irradiation methods, Superlattice. Microst. 51 (2012) 512–522, https://doi.org/10.1016/j.spmi.2012.01.015.
[48] H. Usui, The effect of surfactants on the morphology and optical properties of precipitated wurtzite ZnO, Mater. Lett. 63 (2009) 1489–1492, https://doi.org/10.1016/j.matlet.2009.03.054.
[49] G.N. Narayanan, A. Karthigeyan, Influence of different concentrations of cetyltrimethylammonium bromide on morphological, structural and optical properties of zinc oxide nanorods, Mater. Today Proc. 3 (2016) 1762–1767, https://doi.org/10.1016/j.matpr.2016.04.071.
[50] X.L. Xu, Y. Chen, S.Y. Ma, S.H. Yan, Y.Z. Mao, T. Wang, H.Q. Bian, CTAB-assisted synthesis of unique 3D ZnO and the acetone sensing performances, Mater. Lett. 151 (2015) 5–8, https://doi.org/10.1016/j.matlet.2015.03.017.
[51] H.J. Zhai, W.H. Wu, F. Lu, H.S. Wang, C. Wang, Effects of ammonia and cetyltrimethylammonium bromide (CTAB) on morphologies of ZnO nano- and micromaterials under solvothermal process, Mater. Chem. Phys. 112 (2008) 1024–1028, https://doi.org/10.1016/j.matchemphys.2008.07.020.
[52] B. Wen, Y. Huang, J.J. Boland, Controllable growth of ZnO nanostructures by a simple solvothermal process, J. Phys. Chem. C 112 (2008) 106–111, https://doi.org/10.1021/jp076789i.
[53] H. Zhang, D. Yang, Y.J. Ji, X.Y. Ma, J. Xu, D.L. Que, Low temperature synthesis of flowerlike ZnO nanostructures by cetyltrimethylammonium bromide-assisted hydrothermal process, J. Phys. Chem. B 108 (2004) 3955–3958, https://doi.org/10.1021/jp036826f.
[54] S. Ghosh, V.S. Goudar, K.G. Padmalekha, S.V. Bhat, S.S. Indi, H.N. Vasa, ZnO/Ag nanohybrid: synthesis, characterization, synergistic antibacterial activity and its mechanism, RSC Adv. 2 (2014) 930–940, https://doi.org/10.1039/C1RA00815C.
[55] A. Khorsand Zak, W.H.A. Majid, M. Ebrahimizadeh Abrishami, R. Yousefi, R. Parvizi, Synthesis, magnetic properties and X-ray analysis of Zn0.97X0.03O nanoparticles (X = Mn, Ni, and Co) using Scherrer and size-strain plot methods, Solid State Sci. 14 (2012) 488–494, https://doi.org/10.1016/j.solidstatesciences.2012.01.019.
[56] A.S. Adeleye, J.R. Conway, K. Garner, Y. Huang, Y. Su, A.A. Keller, Engineered nanomaterials for water treatment and remediation: costs, benefits, and applicability, Chem. Eng. J. 286 (2016) 640–662, https://doi.org/10.1016/j.cej.2015.10.105.
[57] E. Gutierrez, Química Inorgánica, Reverté S.A., 1988.
[58] S. Khosravi-Gandomani, R. Yousefi, F. Jamali-Sheini, N.M. Huang, Optical and electrical properties of p-type Ag-doped ZnO nanostructures, Ceram. Int. 40 (2014) 7957–7963, https://doi.org/10.1016/j.ceramint.2013.12.145.
[59] A. Sierra-Fernandez, L.S. Gomez-Villalba, O. Milosevic, R. Fort, M.E. Rabanal, Synthesis and morpho-structural characterization of nanostructured magnesium hydroxide obtained by a hydrothermal method, Ceram. Int. 40 (2014) 12285–12292, https://doi.org/10.1016/j.ceramint.2014.04.073.
[60] X. Fan, H. Zhang, N. Du, P. Wu, X. Xu, Y. Li, D. Yang, Vertically ordered Ni3Si2/Si nanorod arrays as anode materials for high-performance Li-ion batteries, Nanoscale 4 (2012) 5343, https://doi.org/10.1039/c2nr31045g.
[61] X. Zhang, J. Qin, Y. Xue, P. Yu, B. Zhang, L. Wang, R. Liu, Effect of aspect ratio and surface defects on the photocatalytic activity of ZnO nanorods, Sci. Rep. 4 (2014) 4–11, https://doi.org/10.1038/srep04596.
[62] Y. Zheng, L. Zheng, Y. Zhan, X. Lin, Q. Zheng, K. Wei, Ag/ZnO heterostructure nanocrystals: synthesis, characterization, and photocatalysis, Inorg. Chem. 46 (2007) 6980–6986, https://doi.org/10.1021/ic700688f.
[63] D. Lin, H. Wu, W. Zhang, H. Li, W. Pan, Enhanced UV photoresponse from heterostructured Ag–ZnO nanowires, Appl. Phys. Lett. 94 (2009), https://doi.org/10.1063/1.3126045, 172103-1-3.

[64] Y. Lai, M. Meng, Y. Yu, One-step synthesis, characterizations and mechanistic study of nanosheets-constructed fluffy ZnO and Ag/ZnO spheres used for rhodamine B photodegradation, Appl. Catal. B Environ. 100 (2010) 491–501, https://doi.org/10.1016/j.apcatb.2010.08.027.
[65] X. Wang, H. Fan, P. Ren, Self-assemble flower-like SnO2/Ag heterostructures: correlation among composition, structure and photocatalytic activity, Colloids Surf. A Physicochem. Eng. Asp. 419 (2013) 140–146, https://doi.org/10.1016/j.colsurfa.2012.11.050.
[66] O. Lupan, L. Chow, L. Ono, B. Cuemya, G. Chai, H. Khallaf, P. Sanhoon, A Schulte, synthesis and characterization of Ag-or Sb-doped ZnO nanorods by a facile hydrothermal route, J. Phys. Chem. C (2010) 12401–12408.
[67] L. Muñoz-Fernandez, A. Sierra-Fernandez, O. Milošević, M.E. Rabanal, Solvothermal synthesis of Ag/ZnO and Pt/ZnO nanocomposites and comparison of their photocatalytic behaviors on dyes degradation, Adv. Powder Technol. (2016), https://doi.org/10.1016/j.apt.2016.03.021.
[68] T.J. Whang, M.T. Hsieh, H.H. Chen, Visible-light photocatalytic degradation of methylene blue with laser-induced Ag/ZnO nanoparticles, Appl. Surf. Sci. 258 (2012) 2796–2801, https://doi.org/10.1016/j.apsusc.2011.10.134.
[69] J.H. Zeng, B. Bin Jin, Y.F. Wang, Face enhanced photocatalytic effect with uniform single-crystalline zinc oxide nanodisks, Chem. Phys. Lett. 472 (2009) 90–95, https://doi.org/10.1016/j.cplett.2009.02.082.
[70] G. Appierot, A. Lipovsky, R. Dror, N. Perkas, Y. Nitzan, R. Lubart, A. Gedanken, Enhanced antibacterial actiwity of nanocrystalline ZnO due to increased ROS-mediated cell injury, Adv. Funct. Mater. 19 (2009) 842–852, https://doi.org/10.1002/adfm.200801081.
[71] L. Xu, Y.L. Hu, C. Pelligra, C.H. Chen, L. Jin, H. Huang, S. Sithambaram, M. Aindow, R. Joesten, S.L. Suib, ZnO with different morphologies synthesized by solvothermal methods for enhanced photocatalytic activity, Chem. Mater. 21 (2009) 2875–2885, https://doi.org/10.1021/cm900608d.
[72] W.L. Ong, K.W. Yew, C.F. Tan, T.K. Tan Adrian, M. Hong, G.W. Ho, Highly flexible solution processable heterostructured zinc oxide nanowires mesh for environmental clean-up applications, RSC Adv. 4 (2014) 27481–27487, https://doi.org/10.1039/C4RA03951C.
[73] M.S. Lee, S.S. Hong, M. Mohseni, Synthesis of photocatalytic nanosized TiO2-Ag particles with sol-gel method using reduction agent, J. Mol. Catal. A Chem. 242 (2005) 135–140, https://doi.org/10.1016/j.molcata.2005.07.038.
[74] M. Rabbani, J. Shokraiyan, R. Rahimi, R. Amrollahi, Comparison of photocatalytic activity of ZnO, Ag-ZnO, Cu-ZnO, Ag, Cu-ZnO and TPPS/ZnO for the degradation of methylene blue under UV and visible light irradiation, Water Sci. Technol. 84 (2021) 1813–1825, https://doi.org/10.2166/wst.2021.360.
[75] H.R. Liu, G.X. Shao, J.F. Zhao, Z.X. Zhang, Y. Zhang, J. Liang, X.G. Liu, H.S. Jia, B. S. Xu, Worm-like Ag/ZnO core-shell heterostructural composites: fabrication, characterization, and photocatalysis, J. Phys. Chem. C 116 (2012) 16182–16190, https://doi.org/10.1021/jp2115143.
[76] J. Wang, X. Zhang, Twinning effects on strength and plasticity of metallic materials, MRS Bull. 41 (2016) 274–281, https://doi.org/10.1557/mrs.2016.67.
[77] Y. Wang, S. Liu, C. Pei, Q. Fu, Z.J. Zhao, R. Mu, J. Gong, Modulating the surface defects of titanium oxides and consequent reactivity of Pt catalysts, Chem. Sci. 10 (2019) 10531–10536, https://doi.org/10.1039/c9sc03119g.